A Method to Include Single Photon Events in Image Reconstruction for a 1 mm Resolution PET System Built with Advanced 3-D Positioning Detectors

Garry Chinn, *Member, IEEE*, Angela M. K. Foudray, *Student Member, IEEE*, and Craig S. Levin, *Member, IEEE*

***Abstract*–We are developing cadmium zinc telluride detectors with three-dimensional photon positioning capabilities for high-resolution PET imaging. These detectors exhibit high spatial resolution (1 mm), energy resolution (2.5% full width at half maximum for 511 keV photons), and the ability to resolve individual Compton interactions within the detector. Using these measurements, non-coincident single photons can be reconstructed by estimating the incoming direction of the photon using the kinematics of Compton scatter within the detector. In this paper, we investigated image reconstruction methods for combining two different types of measurements: conventional coincidence photon events and non-coincident single photon events. We introduce a new image reconstruction method that uses a Bayesian projector function. Using Monte Carlo simulated data generated by GATE (Geant4), we showed that this new approach has the potential to improve contrast and resolution with comparable signal-to-noise ratio.**

I. Introduction

CONVENTIONAL positron emission tomography (PET) systems use coincidence measurements to reconstruct images. The position of decay events in tissue lies along the line between a measured pair of photons detected in coincidence. In Compton PET, a Compton camera [1]-[3] produces images from measurements of single photons. A Compton camera typically uses a scattering layer and an absorption layer. By recording the position and energy of a Compton interaction in the scatter layer and a photoelectric interaction in the absorption layer, the kinematics of Compton scatter, or simply "Compton kinematics," can position the decay event somewhere on a cone-surface.

Hybrid Compton PET systems using two Compton cameras with coincidence capability [4] have also been proposed. Such systems are able to perform both conventional coincidence PET imaging and Compton kinematics imaging.

Some three-dimensional (3-D) PET detectors [5]-[8] also have the ability to function as a coincidence detector and as a Compton camera. A 3-D detector can perform coincidence Compton kinematics collimation on single photons if it can precisely measure the position and energy of individual interactions in the detector.

Manuscript received November 16, 2006. This work was supported in part by NIH grants NCI R21 CA098691, NIBIB R33 EB003283, and NCI R01 CA119056.

G. Chinn, A. M. K. Foudray and C. S. Levin are with the Dept. of Radiology, Stanford School of Medicine, Stanford, CA 94305 USA. (G. Chinn's contacts: tel: 650-736-7218, e-mail: gchinn@stanford.edu).

With current technology, Compton kinematics collimation suffers from poor angular blurring due to Doppler broadening, energy blurring, and position blurring. Therefore, the reconstructed spatial resolution of Compton kinematics collimation is limited compared to coincidence collimation. Combining Compton kinematics collimation with coincidence collimation to produce better images is a challenging problem because of this large resolution mismatch.

In this work, we investigate image reconstruction methods that can combine Compton kinematics measurements of non-coincident singles with coincidence measurements.

II. Theory

A. Compton Kinematics in a 3-D Detector

In conventional PET, images are reconstructed from coincidence events, which occur when exactly two photons are detected within a time coincidence window. The *projector function* for a coincidence event is the line between the two detectors that recorded the photons. A 3-D PET detector that can measure the position and energy of individual interactions can use Compton kinematics to calculate a *Compton kinematics cone-surface projector function* for non-coincident single photons.

For this discussion, we apply different image reconstruction strategies to Monte Carlo simulations of a 3-D cadmium zinc telluride (CZT) cross-strip detector that we are currently developing [5]. The general theory described here is applicable to other 3-D detectors or Compton cameras with coincidence capabilities.

CZT is a semiconductor that directly converts high-energy photons into electrical signals. In our design, shown in Fig. 1, anode and cathode cross strips sample the interaction position along two dimensions. The position in the third dimension is computed from the anode-to-cathode signal ratio. A 1 mm x 1 mm x 1 mm spatial resolution can be achieved by using 1 mm pitch anode and cathode orthogonal cross strips. The energy resolution has been measured at ≤2.5% FWHM for 511 keV photons [5]. These CZT detectors are then stacked in an edge-on configuration to provide high intrinsic detection efficiency as well as facilitate coupling to readout electronics. With a minimum photon traversal distance of 4 cm, the single 511 keV photon detection efficiency is roughly 86% (74% for two photons in coincidence).

1-4244-0561-0/06/$20.00 ©2006 IEEE.

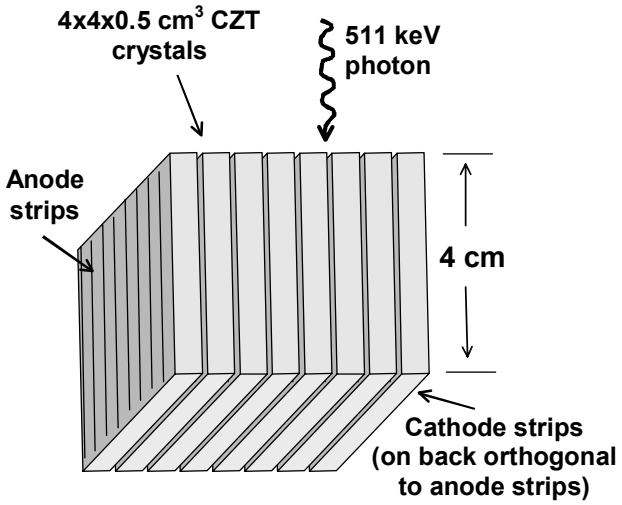

Fig. 1. The 3-D CZT detector with orthogonal cross-strip anodes and cathodes is shown. The detector is oriented edge-on to facilitate coupling to readout electronics with a minimum photon traversal path of 4 cm for high photon detection efficiency. With 1 mm pitch anode and cathode strips, the detector achieves 1 mm^3 spatial resolution with an energy resolution of 2.5% FWHM for 511 keV photons [5].

Fig. 2 illustrates how a high-resolution 3-D detector can calculate the incident angle of a single photon event. The incident angle of the photon can be estimated when the position and energy of the first two interactions in the detector are measured. Monte Carlo simulations with GATE (GEANT4) [9] suggest that 70% of all detected events involve two or more interactions in the detectors. A cone-surface projector function is then formed for the single photon event where the line formed by the two interactions form the cone axis and the cone half angle φ is calculated by

$$\cos\varphi = 1 - m_e c^2 \left(\frac{1}{E_1} - \frac{1}{E_0} \right) \tag{1}$$

where E_0 is the incident photon energy and E_1 is the photon energy after the first Compton interaction in the detector, m_e is the mass of an electron, and c is the speed of light. Doppler broadening, energy blurring, and spatial blurring in the 3-D detector leads to angular blurring of the cone half angle φ.

The forward model for reconstructing these single events is given as

$$s(y_i, \phi_i) = \int_C p(\phi_i, y_i, x) f(x;T) dx \tag{2}$$

where $f(x) \equiv f(x;T)$ is a random variable corresponding to the number of photons generated over the total scan time T at the point x and $p(\phi_i, y_i, x)$ is the probability of an emission from position x in tissue detected at y_i and incident angle ϕ_i.

Compton kinematics can provide greater information when three or more interactions occur [10]. We did not investigate this case, limiting this investigation to the Compton kinematics projector cone-surface calculated using only the first two interactions.

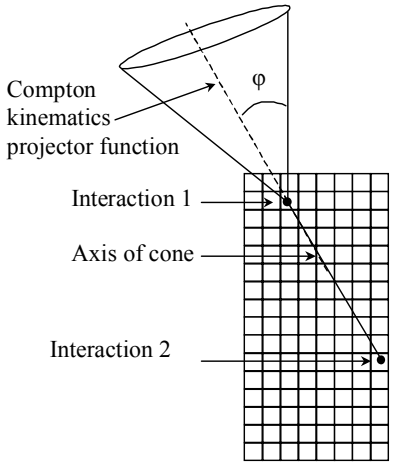

Fig. 2. A schematic of Compton kinematics is shown for the 3-D CZT detector. The spatial location of two interactions in the detector determines the axis of the cone. The measured energy of the interactions determines the angle of the cone.

B. Coincidence Events Model

In conventional PET, a coincidence event occurs when exactly two photons are detected in the photopeak energy window and coincidence time window. Let y_{kl} correspond to the *k*-th and *l*-th detector pair, then the counts recorded for this pair is given by

$$o(y_{kl}) = \int_L p(y_{kl}, x) f(x;T) dx \tag{3}$$

where $f(x) \equiv f(x;T)$ is a random variable corresponding to the number of photons generated over the total scan time T at the point x and $p(y_{kl}, x)$ is the fraction of annihilation events at position x in tissue that result in a pair of photons detected in coincidence recorded at the detector pair y_{kl}.

C. List-mode Reconstruction Algorithm

In this study, list-mode algorithm was used to reconstruct the images. In the list-mode approach, a histogram of the counts is not used. Instead, the measurements $\mathbf{m} = \{m_i\}, m_i \in \{o(y_{ij}), s(y_k, \phi_k)\}$ correspond to the sequence of individual detected events. The expectation maximization algorithm (EM) [11] can be used to reconstruct the image with voxels λ_j using the iteration

$$\lambda_j^{l+1} = \frac{\lambda_j^l}{n_j} \sum_i \frac{m_i p_{ij}}{\sum_k p_{ik} \lambda_k^l} \tag{4}$$

where l is the previous iteration number, n_j represents the sensitivity correction for the *j*-th voxel, and p_{ij} represents the discrete weights of the projector function for the *j*-th voxel and measurement m_i. If m_i is a non-coincident singles event, then p_{ij} is calculated from the discrete version of (2). Otherwise, m_i is a coincidence event and a discrete version of

(3) is used to form p_{ij}. This algorithm is readily adapted for list mode data [12], [13].

Ordered subsets [14] can accelerate the image reconstruction process to form a list mode ordered subset EM algorithm (LM OS-EM). In this approach, the list-mode data set is divided into *S* equal length data sets. The image is then updated after each subset before the next data subset is processed. Each iteration pass through the entire data set then results in *S* image updates, accelerating the reconstruction process.

For each list-mode count, a coincidence window is applied followed by a clustering method to group interactions. Each cluster corresponds to the energy deposited by a single photon. Next, an energy window is used to reject photons that may have been scattered in tissue. If two clusters are accepted after the energy window, sequence estimation is used to identify the first interaction for each photon. The coincidence line projector function is used for p_{ij} with the ends of the line segment positioned at the location of the first interaction for each photon.

For non-coincident single photon events, sequence estimation is used to identify the first two interactions. The first two interactions are then used to calculate the Compton kinematics projector function, forming the values of p_{ij} used by (5).

D. Simultaneous Data Channels

We refer to techniques for combining different types of measurements for image reconstruction as multi-channel tomography. The coincidence events form one data channel with high-reconstructed spatial resolution. The non-coincident singles events form a second channel with low reconstructed spatial resolution. The objective is to combine these channels to produce an image with superior quality in terms of contrast, resolution, and/or signal-to-noise ratio. We investigated three different reconstruction methods.

In the simultaneous data channel approach, the Poisson-distributed data vector is a combination of coincidence and non-coincident singles events given by

$$\mathbf{m} = \begin{pmatrix} o(y_{ij}) \\ s(y_k, \phi_k) \end{pmatrix}. \tag{5}$$

The system matrix is then formed by discrete approximations to (2) and (3).

E. Sequential Data Channels

In the sequential data channel approach, the coincidence and non-coincident singles events are used separately in the reconstruction process. Starting from a uniform image, the OS-EM algorithm is performed using only the non-coincident singles data. OS-EM iterations are then continued using only the coincidence data. Only a single iteration can be performed using this approach.

F. Bayesian Projector

In conventional image reconstruction, the line projector function assumes that the probability of the emission event is uniform along the line of response. In the Bayesian projector approach, an *a priori* image is used to re-weight the line projector such that the probability along of the line of response is proportional to the expected activity. Let $g(x) \equiv g(x;T)$ be the image prior, the probability that a photon is generated over the total scan time *T* at the point *x*. The Bayesian line projector function for coincidence data is then given by

$$o(y_{kl}) = \int_L p(y_{kl}, x) g(x;T) f(x;T) dx . \tag{6}$$

Similarly, a Bayesian projector function for non-coincident singles event is given by

$$s(y_i, \phi_i) = \int_C p(\phi_i, y_i, x) g(x;T) f(x;T) dx . \tag{7}$$

For multi-channel tomography, one data channel is used to generate a prior that is used to modify the projector function for the reconstruction of the other channel. In this study, we reconstructed the non-coincidence singles data to produce the prior image. The Bayesian projector is used to reconstruct the coincidence events, producing the final image.

G. Sources of Errors

The accuracy of the Compton kinematics projector function is affected by a number of factors. Detectors have limited energy and spatial resolution. Positioning uncertainty blurs the orientation of the cone axis and noise in the energy measurement blurs the cone angle. These effects degrade the spatial resolution of images reconstructed from single events.

Another error occurs when a scattered photon does not completely deposit its total energy into the detectors. If the photon scatters twice but does not undergo photoelectric absorption in a detector, only a fraction of the total photon energy will be measured. As a result, the Compton kinematics calculation will be incorrect, leading to blurring of the calculated cone angle. This type of error is expected to reduce the resolution of the reconstructed image.

The Compton scattering formula assumes that the electron is free and at rest before the interaction. The momentum of bound electron will alter the scattering direction. This effect is called Doppler broadening since the electron momentum adds a Doppler shift to the scattering direction. This effect will add angular blur to the Compton kinematics projector function leading to resolution loss in the reconstructed image.

Another type of error results in a rare occasion when two interactions occur in the same strip of the same device. In this case, each individual interaction cannot be resolved independently. The centroid of the positions and the total energy is recorded as a single interaction. Consequently, multiple Compton interactions occurring in the same strip of the same device will lead to an incorrect cone axis and cone angle. Fortunately, the probability that two or more

interactions occur in the same strip of the same detector device is relatively low.

Finally, an error results when the identity and sequence of the first two interactions within the detector are incorrectly estimated. Given the limited time resolution of current detector technology [5], the order of interactions cannot be directly measured. The interaction sequence must be estimated using the positions and energies of the interactions. Incorrect ordering will produce errors in both the orientation of the cone axis and the cone angle. This type of error is expected to reduce the reconstructed image contrast.

These errors and their effects are summarized in Table 1.

TABLE 1. TYPES OF ERRORS IN COMPTON KINEMATICS PROJECTOR FUNCTION

Cause of Error	Reconstructed Image Effect
Detector spatial positioning	Resolution loss
Detector energy blur	Resolution loss
Photon deposits partial energy	Resolution loss
Doppler broadening	Resolution loss
Multiple interactions in one detector cross-strip	Contrast loss
Incorrect interactions sequencing	Contrast loss

III. METHODS AND RESULTS

A. Monte Carlo Simulations by GATE

We performed simulations of PET systems built using the proposed cross-strip CZT detectors. The Monte Carlo simulation package GATE (GEANT4) [9] was used. With GATE, we simulated a phantom for a box-shaped small animal PET system built using the proposed cross-strip CZT detectors [5]. We assumed that the detectors had a 1 mm x 1 mm x 1 mm spatial resolution with 3% energy resolution FWHM for 511 keV photons. We assumed that the energy resolution FWHM was $3\% * \sqrt{511/e_{pho}}$ where e_{pho} is the energy of the photon in keV. A schematic of the system is shown in Fig. 3, which has 8 cm x 8 cm transaxial FOV. The axial length of the simulated system in this paper was 2 cm. Data acquisition was simulated for 7 non-overlapping bed positions. GATE was used to generate hits files of all the individual interactions within the detectors. We processed these files to simulate the performance of the system.

We simulated a resolution phantom that was a 5 cm diameter, water-filled cylinder with a single plane of spherical sources divided into four quadrants. The spherical sources in each quadrant were 1, 1.25, 1.5, and 1.75 mm in diameter with center-to-center separation that was twice the diameter of the spheres. A total of 0.2 mCi of activity was simulated. Images reconstructed using the coincidence data and non-coincident singles data are shown in Fig. 4.

Images reconstructed using the same data set by the various methods are shown in Fig. 5. Reconstruction using only the coincidence data is shown in the top left figure. There is no discernible difference in the image quality between simultaneous channel (top right), sequential channel (bottom left), and coincidence-only images. The noise structure for the simultaneous channel approach differs from the coincidence-only reconstructed image. The noise structure is visually identical for sequential channel and coincidence-only image reconstruction. The Bayesian projector approach (bottom right) produced an image with improved contrast against the background compared to the other methods.

The mean and variance images were computed from 20 simulated trials for each of the methods. The mean images are shown in Fig. 6. The image quality is comparable for coincidence-only (top left), simultaneous channel (top right), and sequential channel (bottom left) images. The mean reconstructed image for the Bayesian projector method shows a larger partial volume effect for the 1 mm spheres.

The variance-to-signal ratio was computed from 20 trials for regions of interests (ROI) drawn around the spheres on the center plane. The results are tabulated in Table 2. The simultaneous channel methods showed the best noise performance and the Bayesian projector approach had the worst performance.

The peak-to-valley ratio was measured from the mean images and plotted for the different reconstruction methods and shown in Fig. 7. Shown are the peak-to-valley ratios for the various sized spheres. The Bayesian projector approach had a better peak-to-valley ratio for all sized spheres.

The resolution for the various methods was calculated by drawing profiles through the various sized spheres in the mean reconstructed image. A Gaussian function was fitted to the profiles and the full width at half maximum (FWHM) for the various sized spheres are plotted in Fig. 8. The Bayesian projector method showed better contrast and resolution for all size spheres than the other methods with a slight loss in signal-to-noise ratio.

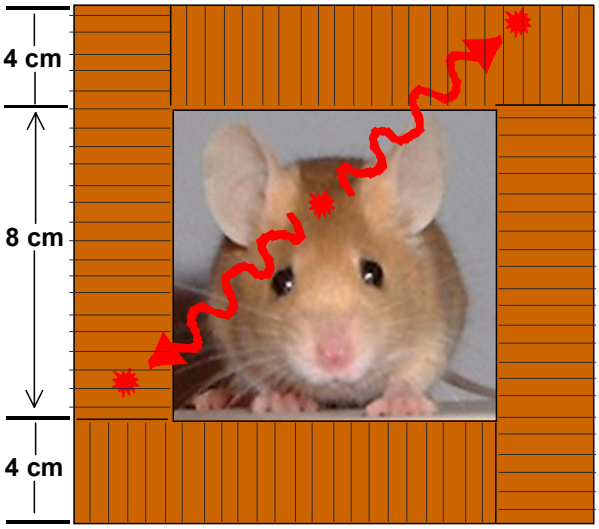

Fig. 3. The small animal imaging system geometry is illustrated. The system has an 8 cm x 8 cm field of view with a crystal thickness of 4 cm.

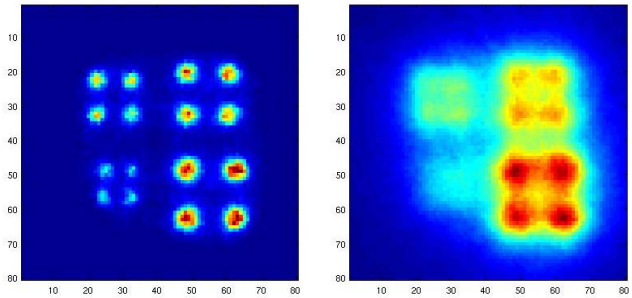

Fig. 4. A phantom with 16 spherical sources of 1, 1.25, 1.5, and 1.75 mm in diameter was simulated with GATE. Reconstructed images of the phantom are shown for (left) coincidence data and (right) non-coincident singles data.

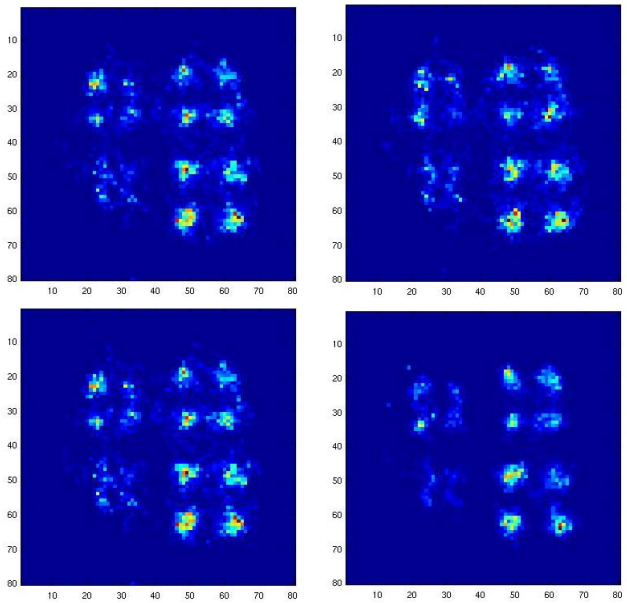

Fig. 5. Shown are images for (top left) coincidence-only, (top right) simultaneous coincidence + singles, (bottom left) sequential coincidence then singles, and (bottom right) Bayesian projector image reconstruction.

TABLE 2. VARIANCE-TO-SIGNAL RATIO FOR RECONSTRUCTION METHODS IS SHOWN WITH RESULTS NORMALIZED TO COINCIDENCE-ONLY RECONSTRUCTION

Method	Variance-Mean Ratio
Coincidence-only	1.00
Simultaneous Channel	0.93
Sequential Channel	1.01
Bayesian Projector	1.35

IV. DISCUSSION AND CONCLUSIONS

The results presented in this study are a work-in-progress. We are continuing to incorporate the effects of Doppler broadening into our simulations. Further, we will investigate more complex phantoms including those with background activity and a higher singles to coincidence photon ratio where there will likely be further improvements in signal-to-noise ratio when singles are added to the coincidence data statistics. More detailed quantitative analysis of the methods is still needed.

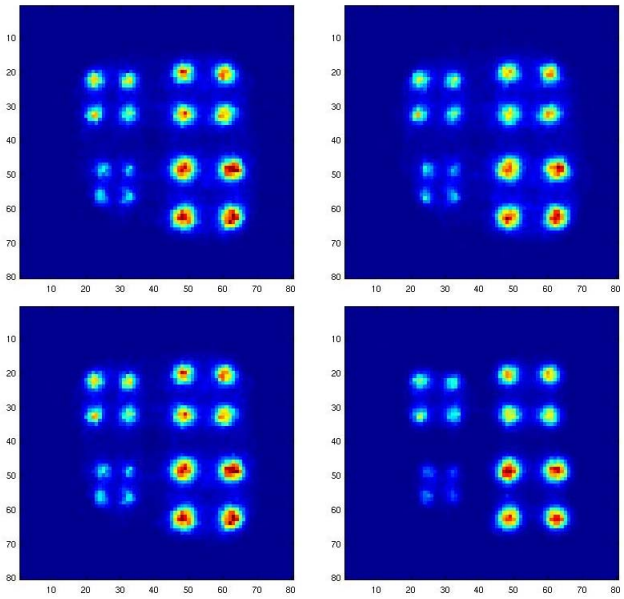

Fig. 6. Shown are the mean reconstructed images for (top left) coincidence-only, (top right) simultaneous, (bottom left) sequential, and (bottom right) Bayesian projector image reconstruction.

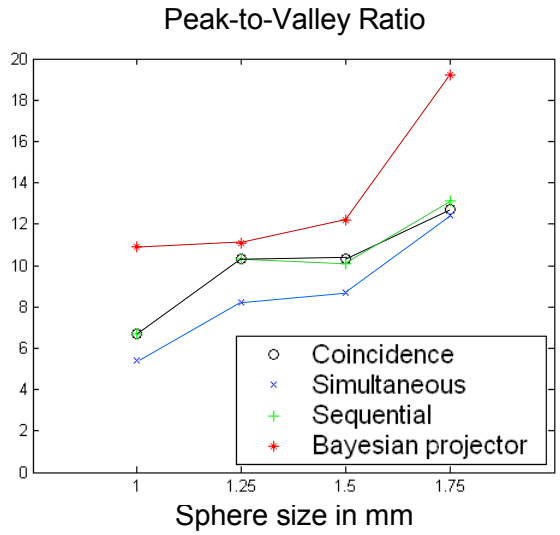

Fig. 7. A plot of the peak-to-valley ratio for the various reconstruction methods is shown for the various sized spheres.

Based on this preliminary study, we found that there was no significant difference in resolution, contrast, and signal-to-noise ratio between coincidence-only, simultaneous channel, and sequential channel image reconstruction methods. Although the current implementation has problems, the Bayesian projector approach is a promising direction.

The Bayesian projector approach showed improved resolution and contrast however, there is one main shortcoming with this technique. The images produced by the Bayesian projector function depend on the quality of the image prior and the phantom characteristics.

For the Bayesian projector approach, the non-coincident singles were used to generate a prior. The low-resolution nature of this image leads to partial volume effects for the 1 mm spheres. This partial volume effect results in a lower probability of counts placed in the 1 mm spheres by the

Bayesian projector function. Consequently, the reconstructed activity in the 1 mm spheres was biased down proportionately to the partial volume effect of the reconstructed image used to generate the prior. Effectively, counts were "stolen" from the 1 mm spheres and placed in the other spheres. Misplaced counts could explain the observed decrease in the signal-to-noise ratio for the Bayesian projector method.

Therefore, we are continuing to investigate post-processing methods on the prior image to reduce biasing effects caused by partial volume effects. We are currently exploring various methods that will set the local maxima in the prior image to the same magnitude.

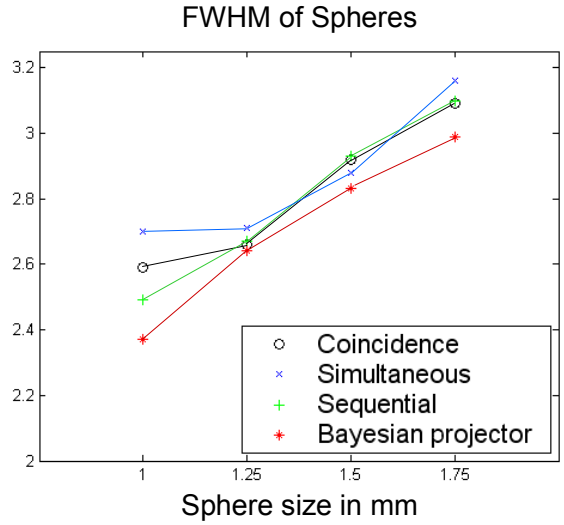

Fig. 8. A plot of the FWHM of a Gaussian fitted to profiles drawn through the spheres.

REFERENCES

[1] D.B. Everett, J.S. Fleming, R.W. Todd, and J.M. Nightingale, "Gamma-radiation imaging system based on the Compton effect," *Proc. IEE*, vol. 124, pp. 995-1000, 1977.

[2] M. Singh, "An electronically collimated gamma camera for single photon emission computed tomography, Part I: Theoretical considerations and design criteria," *Med. Phys.*, vol. 10, pp. 421-427, 1983.

[3] M. Singh and D. Doria, "An electronically collimated gamma camera for single photon emission computed tomography, Part II: Image reconstruction and preliminary experimental measurements," *Med. Phys.*, vol. 10, pp. 428-435, 1983.

[4] J.E. Gillam, T.E. Beveridge, R.A. Lewis, "Positron emission imaging using acquired cone-surfaces from opposing Compton cameras," 2004 IEEE Nuc. Sci Symposium Conf. Rec., vol. 5, pp. 2810-2814, 2004.

[5] [5] Levin CS, Mattesson JL, Skelton RT, Pelling MR, Duttweiler F, Huszar G, LeBlanc PC. Promising characteristics and performance of cadmium zinc telluride for positron emission tomography. 2004 Nuclear Science Symposium and Medical Imaging Conference, Rome Italy, 2004. Abstract # M2-117, Book of Abstracts, p. 136, IEEE Nuclear and Plasma Science Society.

[6] Y.F. Du, Z. He, G.F. Knoll, D.K. Wehe, and W. Li, "Evaluation of a Compton scattering camera using 3-D position sensitive CdZnTe detectors," Nuc. Instr. Methods Phys. Res. A, vol. 457, pp. 203-211, 2001.

[7] C.E. Lehner, Z. He, F. Zhang, "4π Compton imaging using a 3-D position-sensitive CdZnTe detector via weighted list-mode maximum likelihood," *IEEE Trans. Nuc. Sci.*, vol. 51, no. 4, pp. 1618-1624, 2004.

[8] A. Braem, M. Chamizo Llatas, E. Chesi, J.G. Correia, F. Garibaldi, C. Joram, S. Mathot, E. Nappi, M. Riberio da Silva, F. Schoenahl, J. Seguinot, P. Wieilhammer, and H. Zaidi, "Feasibility of a novel design of high resolution parallax-free Compton enhanced PET scanner dedicated to brain research," *Phys. Med. Biol.* vol. 49, 2547-2562, 2004.

[9] S. Jan, G. Santin, D Strul, S. Staelens, K. Assié, D. Autret, S. Avner, R Barbier, M. Bardiès, PM Bloomfield, D. Brasse, V. Breton, P. Bruyndonckx, I. Buvat, A.F. Chatziioannou, Y. Choi, Y.H. Chung, C. Comtat, D. Donnarieix, L. Ferrer, S.J. Glick, C.J. Groiselle, D. Guez, P.F. Honore, S. Kerhoas-Cavata, A.S. Kirov, V. Kohli, M. Koole, M. Krieguer, D.J. van der Laan, F. Lamare, G. Largeron, C. Lartizien, D. Lazaro, M.C. Maas, L. Maigne, F. Mayet, F. Melot, C. Merheb, E. Pennacchio, J. Perez, U. Pietrzyk, F.R. Rannou, M. Rey, D.R. Schaart, C.R. Schmidtlein, L. Simon, T.Y. Song, JM. Vieira, D. Visvikis, R. Van de Walle, E. Wieërs, C. Morel, "GATE: a simulation toolkit for PET and SPECT," *Phys. Med. Biol.* vol. 49, 4543-4561, 2004.

[10] N. Dogan, D.K. Wehe, and A.Z. Akcasu, "A source reconstruction method for multiple scatter Compton cameras," *IEEE Trans. Nuc. Sci.*, vol. 39, no. 6, pp. 1427-1430, 1992.

[11] L.A. Shepp and Y. Vardi, "Maximum likelihood reconstruction for emission tomography," IEEE Trans. Med. Imaging, vol. 1., pp. 113-122, 1982.

[12] L. Parra and H.H. Barrett, "List mode likelihood: EM algorithm and image quality estimation demonstrated on 2-D PET," *IEEE Trans. Med. Imaging* pp. 228-235, 1998.

[13] S.J. Wilderman, N.H. Clinthorne, J.A. Fessler, C-H Hua, W.L. Rogers, "List mode EM reconstruction of Compton scatter camera images in 3-D," *Proceedings of the 1998 IEEE Nuclear Science Symposium*, vol 3, p1716-1720, 1998.

[14] H.M. Hudson and R.S. Larkin, "Accelerated image reconstruction using ordered subsets of projected data," *IEEE Trans. Med Imaging*, vol. 13, pp. 601-609, 1994.